Nano Research

Open Access

Research Article

Thermosensitive crystallization-boosted thermoelectric hydrogels for self-powered sensing and intelligent perception applications

Pengyuan Kang[1], Yuke Zhang[1], Qiuxi Sun[2], Ziyan Lu[1], Yalong Wang[1] ✉, Hu Liu[1] ✉, Chuntai Liu[1], and Changyu Shen[1]

[1] *Key Laboratory of Structural Analysis, Optimization and CAE Software for Industrial Equipment, National Engineering Research Center for Advanced Polymer Processing Technology, Zhengzhou University, Zhengzhou 450002, China*
[2] *School of Kinesiology and Physical Education, Zhengzhou University, Zhengzhou 450002, China*

Cite this article: *Nano Research*, **2026**, *19*, 94908553. https://doi.org/10.26599/NR.2026.94908553

ABSTRACT: Wearable sensing technology has seen widespread use in health monitoring, environmental perception, and human–machine interaction. Among them, sensors that can actively harvest energy from their application scenarios to achieve self-powering are especially favored. In this study, we developed a polyacrylic acid (PAA)-based ionic thermoelectric hydrogel of PAA-$K_3Fe(CN)_6$/$K_4Fe(CN)_6$-guanidinium chloride (GdmCl) hydrogel (PFGH). Under temperature difference driving, redox reactions within the hydrogel directly convert thermal energy into electrical signals. The introduction of GdmCl induces $K_4Fe(CN)_6$ to form thermosensitive crystals, significantly enhancing entropy differences between redox couples. This design enables PFGH to achieve a high thermopower of 3.76 mV·K^{-1} and a normalized power output density of 37.77 mW·m^{-2}·K^{-2}. Additionally, hydrogen bonding between PAA and $[Fe(CN)_6]^{3-/4-}$ ions enable PFGH with excellent mechanical properties (tensile strength of 90 kPa, and elongation at break of 920%). With excellent thermoelectric and mechanical properties, PFGH demonstrates outstanding application potential in wearable sensing fields, achieving diversified functions including self-powered motion monitoring, real-time respiratory status perception, intelligent fire warning, and machine learning-assisted material identification. This study paves the way for next-generation self-powered wearable devices and unlock new possibilities for body heat utilization in smart sensing applications.

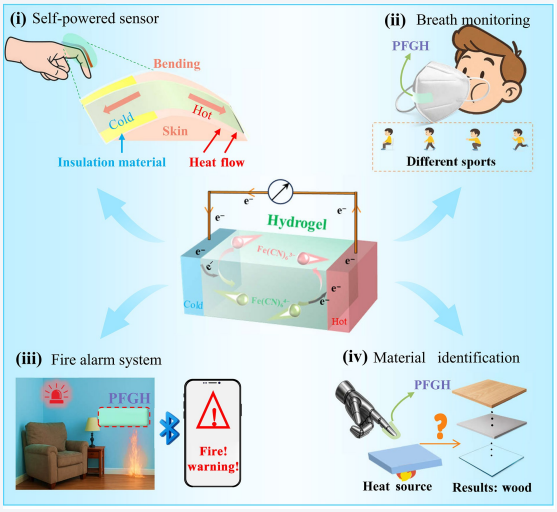

KEYWORDS: thermoelectric hydrogel, thermosensitive crystallization, self-powered sensing, fire warning, material identification

1 Introduction

With the continuous development of digital lifestyle, intelligent wearable technology, as an important branch of technological innovation, is rapidly integrating into practical application scenarios such as health monitoring, intelligent control, and human–machine interaction [1–4]. However, most current wearable devices still heavily rely on traditional battery power supply, leading to increased system weight and structural complexity, and significantly limiting the device's endurance and user wearing comfort [5]. The temperature of human surface tissue is maintained at approximately 36 °C, which can generate a stable temperature difference of ~ 11 °C compared to ambient temperature (25 °C) [6]. The continuous and stable energy generated by the human body provides new insights for solving the energy problems of wearable devices.

Thermoelectric devices based on the thermoelectric effect can effectively utilize the temperature difference between the human body and environment to generate electrical energy for self-powered driving of wearable devices [7, 8]. The thermoelectric performance of thermoelectric devices is typically quantified by the thermopower ($S = -\Delta V/\Delta T$), which reflects the ability of thermoelectric materials to generate potential differences under unit temperature differences and is also an important parameter for

Received: January 5, 2026; **Revised:** January 30, 2026
Accepted: February 7, 2026

✉Address correspondence to Yalong Wang, yalongwang@zzu.edu.cn; Hu Liu, liuhu@zzu.edu.cn

measuring the sensing capability of thermoelectric temperature sensors [9]. Although conventional inorganic semiconductor thermoelectric materials possess good stability, their *S* values are generally below 400 $\mu V \cdot K^{-1}$, and their fabrication costs are relatively high, making it difficult to meet the requirements of flexible electronics for lightweight, low-cost, and bendable characteristics [10]. In contrast, ionic thermoelectric (i-TE) materials have become a research hotspot in recent years due to their high thermopower up to several $mV \cdot K^{-1}$ and low-cost preparation advantages [11]. As a class of polymers renowned for their hydrophilicity and biocompatibility, hydrogels can effectively load electrolyte solutions and are therefore widely studied in i-TE systems, forming ionic thermoelectric hydrogel systems [12–14]. In this system, hydrogels mainly achieve thermoelectric conversion through the Soret effect of ions and thermal redox reactions [15]. The Soret effect describes the phenomenon in which ions undergo directional movement in response to temperature gradients. Due to the distinct characteristics of anions and cations, their rates of thermal migration vary, resulting in differing ion concentrations on the surfaces of two electrodes. This, in turn, generates potential differences [16–19]. The thermoelectric performance of thermal diffusion hydrogels can be effectively enhanced by regulating the interactions between hydrogel matrix and specific cations/anions in salt ions [20, 21]. Fu et al. [22] utilized the ionic coupling shielding effect between Na^+ and the polyacrylic acid (PAA)/polyethylene oxide (PEO) hydrogel, which enabled the thermal migration rate of Na^+ ions to exceed that of Cl^-. Consequently, the prepared PAA/PEO/NaCl hydrogel achieved a thermopower of 3.26 $mV \cdot K^{-1}$. Although ionic thermal diffusion hydrogels that utilize the Soret effect can generate significant potential differences, they still encounter several challenges in practical applications. The continuous accumulation of ions on electrode surfaces results in electrode polarization, which diminishes the driving force for ion migration and impedes further ion movement. The subsequent charging cycle can only commence after an external load is applied or a capacitor is discharged, and their power supply capacity is limited temporally [23, 24].

Redox-type thermoelectric hydrogels generate potential differences because of the different thermodynamic entropies of cation–anion ion pairs, which undergo reversible electrochemical redox reactions at the hot and cold ends, respectively [25]. On the other hand, ions generated from reactions within the hydrogel are transported to the other side through diffusion, convection, and migration. When a continuous temperature gradient is present, connecting the hydrogel to an external load enables reactions within the hydrogel to persist, thereby continuously outputting stable voltage to external circuits and effectively addressing the critical issue of long-term power supply [26]. Common redox couples include ferrocyanide/ferricyanide ($[Fe(CN)_6]^{4-}/[Fe(CN)_6]^{3-}$ ($[Fe(CN)_6]^{3-/4-}$)), sulfate/sulfite (SO_4^{2-}/SO_3^{2-}), ferric/ferrous ions (Fe^{3+}/Fe^{2+}), copper ions/copper (Cu^{2+}/Cu), and iodide/triiodide (I^-/I_3^-) [27–32]. Among them, the $[Fe(CN)_6]^{3-/4-}$ ion pair has garnered widespread attention from researchers due to its high absolute charge and complex structure, achieving a thermopower of ~ 1.4 $mV \cdot K^{-1}$ under certain conditions [33–35]. To further enhance the *S* of redox-type hydrogels, researchers increased the entropy difference between oxidants and reductants by employing methods such as inducing thermosensitive redox ion crystallization, electrostatic effects, and solvation effects to improve the thermoelectric performance of hydrogels [36–38]. For example, Hong et al. [22] introduced $[Fe(CN)_6]^{3-/4-}$ redox couples into bacterial cellulose (BC) hydrogel and utilized propylene glycol (PG) to induce directional crystallization of $[Fe(CN)_6]^{4-}$, significantly enhancing the thermopower from 1.27 to 2.30 $mV \cdot K^{-1}$. Similarly, Liu et al. [39] modulated the thermoelectric performance of a polyacrylamide (PAAm) hydrogel by introducing nine organic solvents with varying Gutmann donor numbers (DN) into an Fe^{2+}/Fe^{3+} electrolyte. They observed a strong inverse correlation between the solvent's DN and the thermopower, with tetramethyl sulfone achieving the highest value (2.49 $mV \cdot K^{-1}$) by tuning entropy contributions through the regulation of solvation shell size of Fe^{3+} ions. However, salt-doped hydrogels frequently display poor mechanical properties and reduced conductivity [34, 40]. Therefore, developing ionic thermoelectric hydrogels that can simultaneously achieve high thermoelectric performance, stretchability, and conductivity remains a significant challenge.

This study is committed to developing an ionic thermoelectric hydrogel with both excellent mechanical properties and high thermoelectric performance to meet the application requirements of self-powered flexible wearable devices [41]. Polyacrylic acid hydrogel with high water content, three-dimensional porous network, and excellent flexibility was prepared through a one-pot method [22, 42–43]. In this system, $[Fe(CN)_6]^{3-/4-}$ ions acted as redox couples, while guanidinium chloride (GdmCl) was introduced to induce $[Fe(CN)_6]^{4-}$ to form thermosensitive crystals, yielding the composite PAA-$K_3Fe(CN)_6/K_4Fe(CN)_6$-GdmCl hydrogel (PFGH). This strategy effectively amplified the entropy difference between ion pairs, significantly enhanced the thermoelectric properties of PFGH. Ultimately, the system achieved a high thermopower of 3.76 $mV \cdot K^{-1}$ and a normalized power density of 37.77 $mW \cdot m^{-2} \cdot K^{-2}$. Furthermore, the hydrogen bonding interactions between PAA and $[Fe(CN)6]^{3-/4-}$ ions endowed the PFGH with outstanding mechanical properties, demonstrating a tensile strength of 90 kPa and an exceptional elongation at break of 920%. Owing to its superior thermoelectric performance and mechanical characteristics, the PFGH shows great potential for applications in temperature sensing and self-powered strain sensing systems [44]. As illustrated in Fig. 1(a), the system has been successfully demonstrated for multiple applications: human body strain monitoring powered by body heat without external power sources, respiratory parameter tracking during various motion states, multi-channel responsive fire warning devices, and deep learning assisted material identification. This work not only provides a novel technical approach for applying ionic thermoelectric materials in flexible wearable devices but also significantly expands the potential applications of body heat utilization in next-generation intelligent sensing systems.

2 Experimental section

2.1 Materials and chemicals

Acrylic acid (AA), ammonium persulfate (APS), N,N′-methylenebisacrylamide (MBA), potassium ferrocyanide ($K_4Fe(CN)_6 \cdot 3H_2O$), and potassium ferricyanide ($K_3Fe(CN)_6$) were obtained from Aladdin (Shanghai, China). GdmCl was purchased from Shanghai Macklin Biochemical Co., Ltd. and commercial platinum (Pt) sheet/wire electrodes were provided by Xuzhou Xinke Instrument Co., Ltd. All chemicals were used without further purification.

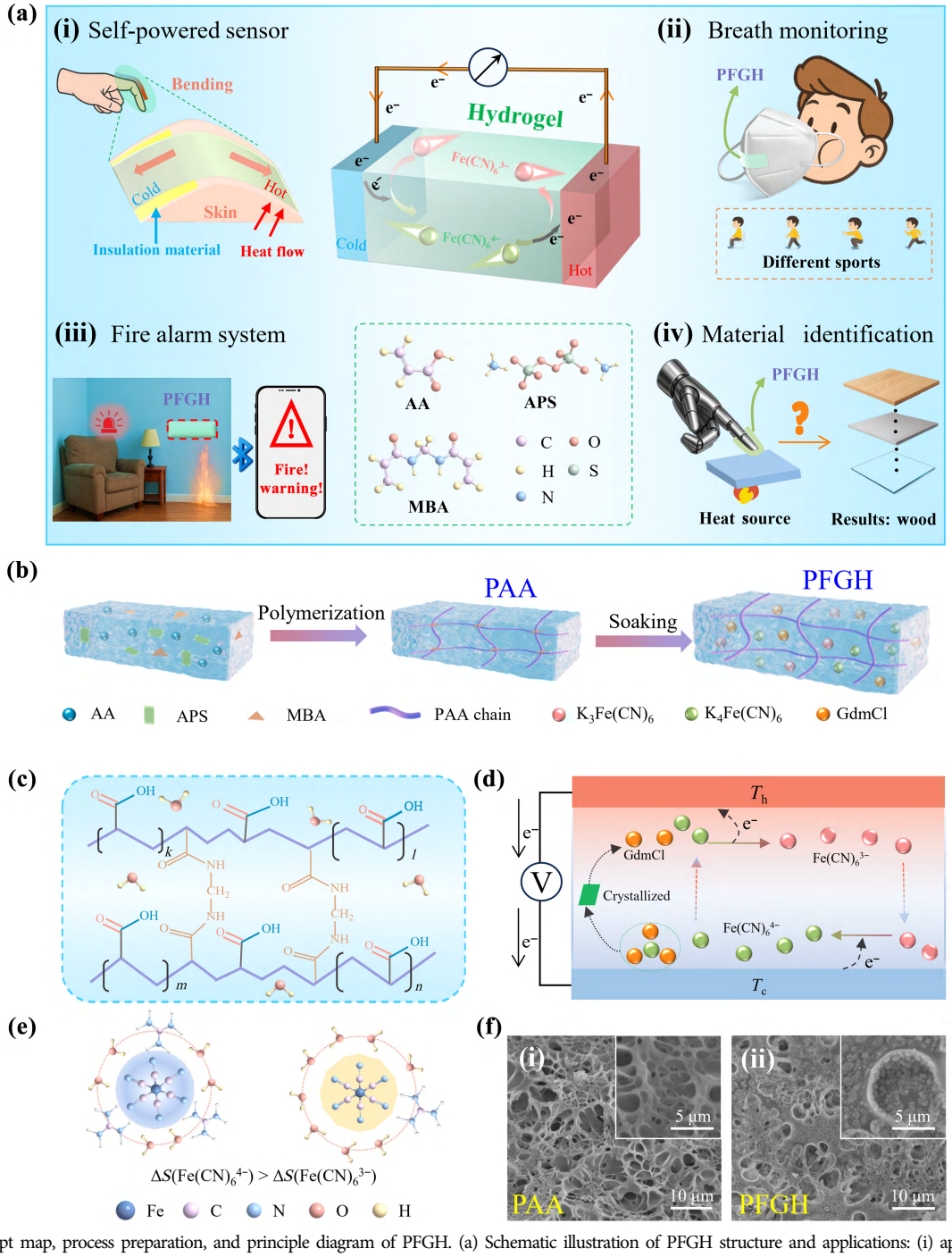

Figure 1 Concept map, process preparation, and principle diagram of PFGH. (a) Schematic illustration of PFGH structure and applications: (i) application of self-powered sensing on human skin, (ii) breathing monitoring under different motion states, (iii) fire alarm system, and (iv) deep learning-assisted material identification. (b) Preparation process of PFGH. (c) Structural schematic of PAA hydrogel. (d) $[Fe(CN)_6]^{3-/4-}$ redox reaction process and Gdm^+ crystallization in PFGH. (e) Solvation shell structure of $[Fe(CN)_6]^{3-/4-}$. (f) SEM images comparing PAA and PFGH.

2.2 Preparation of thermoelectric hydrogel

2.2.1 Preparation of polyacrylic acid hydrogel

The PAA hydrogel was synthesized via free radical polymerization. First, 12 g of AA monomer was dissolved in 30 mL of deionized water under magnetic stirring. Subsequently, 0.78 mL of MBA solution (1 wt.%, prepared by dissolving 0.1 g of MBA in 9.9 g of water) and 0.39 mL of APS solution (10 wt.%, prepared by dissolving 1 g of APS in 9 g of water) were added sequentially as crosslinker and initiator, respectively. After stirring for 30 min, the homogeneous precursor solution was poured into a custom polycarbonate (PC) mold (10 cm × 10 cm) and polymerized at 60 °C for 12 h. The resulting PAA hydrogel (10 cm × 10 cm × 0.2 cm) was carefully removed from the mold, with its appearance shown in Fig. S1(a) in the Electronic Supplementary Material (ESM).

2.2.2 Preparation of PAA-$K_3Fe(CN)_6$/$K_4Fe(CN)_6$ hydrogel (PFH)

PFH was prepared through a solvent exchange method. Equimolar

solutions of $K_3Fe(CN)_6$ and $K_4Fe(CN)_6$ were prepared in deionized water to obtain $[Fe(CN)_6]^{3-/4-}$ solutions with different concentrations (x = 0.1, 0.2, 0.3, and 0.4 M). Pre-cut PAA hydrogel samples were immersed in these solutions for 1 h at room temperature to allow for complete ion exchange. PFH with different $[Fe(CN)_6]^{3-/4-}$ contents was obtained after soaking in different $[Fe(CN)_6]^{3-/4-}$ solutions, and the optical photograph of PFH under optimal concentration is shown in Fig. S1(b) in the ESM.

2.2.3 *Preparation of PAA-$K_3Fe(CN)_6$/$K_4Fe(CN)_6$-GdmCl hydrogel*

The PFGH thermoelectric hydrogel was prepared by solvent exchange and ion-induced crystallization. Equimolar $K_3Fe(CN)_6$ and $K_4Fe(CN)_6$ were dissolved in deionized water and combined with GdmCl to create mixed solutions with varying concentrations (xM $[Fe(CN)_6]^{3-/4-}$-yM GdmCl, where x = 0.1–0.4 and y = 0.1–0.4). Pre-cut PAA hydrogel samples were then immersed in these solutions at 60 °C for 1 h. This process yielded PFGH with different ionic compositions. Figure S1(c) in the ESM displays the optical image of the PFGH prepared at the optimal ionic concentration.

2.3 PFGH device and array assembly

PFGH device fabrication: Rectangular PFGH strips (40 mm × 10 mm × 2 mm) were prepared as the thermoelectric elements. Pt wire electrodes (l = 3.5 mm and d = 0.1 mm) were tightly inserted at both ends of each strip, maintaining a fixed interelectrode distance of 3 cm. To minimize performance degradation from water evaporation, the entire assembly was hermetically sealed using medical adhesive tape.

PFGH array construction: For series-connected devices, PFGH strips (30 mm × 8 mm × 2 mm) were prepared and interconnected using identical Pt wire electrodes (l = 3.5 mm and d = 0.1 mm). A five-element array was constructed by connecting the strips in series configuration. The complete array was then encapsulated with medical tape to enhance long-term water retention capability and ensure operational stability.

2.4 Characterization

Scanning electron microscopy (SEM, JEOL JSM7500F, Japan) operating at 5 kV was employed to examine the cross-sectional morphologies of freeze-dried PAA, PFH, and PFGH. The chemical structures of PAA, PFH, and PFGH were noted with an attenuated total reflection Fourier transform infrared (FTIR) spectrometer (Nicolet 6700). Mechanical properties were assessed at room temperature using a universal testing machine (UTM2203, Shenzhen Sun Technology Co., Ltd., China). The PAA, PFH, and PFGH samples were prepared as rectangular strips with dimensions of 20 mm × 10 mm × 2 mm. Uniaxial tensile experiments were conducted with an initial grip separation of 10 mm and a constant strain rate of 50 mm·min^{-1}. Electrochemical impedance spectroscopy and cyclic voltammetry measurements of hydrogels were conducted on an electrochemical workstation (CHI660E, Shanghai Chenhua, China). A DAQ970A data acquisition system (Keysight Technologies Co., Ltd.) was used to record the thermoelectric voltages of PFGH devices under different temperature differences and resistance or current changes under tensile conditions. A 2450 Digital Source Meter (Tektronix, USA) was used for precise output power testing. The different temperature differences (ΔT) were provided by a TLTP-FW-TEC-XZ semiconductor temperature controller and Peltier devices powered by a programmable linear DC power supply (Victory 3722, Shenzhen Yisheng Victory Technology Co., Ltd.). Temperature monitoring was achieved using K-type thermocouples (Guangzhou Kaipusen Technology) complemented by thermal imaging via an E60 infrared camera (FLIR Systems).

3 Results and discussion

The preparation process of PFGH is illustrated in Fig. 1(b). Initially, free radical polymerization is conducted using acrylic acid as the monomer, MBA as the crosslinker, and APS as the initiator to obtain the initial PAA hydrogel network structure (Fig. 1(c)). Subsequently, the PAA hydrogel is immersed in a mixed ionic solution containing $[Fe(CN)_6]^{3-/4-}$ and GdmCl, allowing for solution exchange to form the PFGH. During this process, a concentration gradient drives the diffusion of $[Fe(CN)_6]^{3-/4-}$ and GdmCl ions into the PAA network. Simultaneously, hydrogen bonds form between the introduced ions and the carboxyl groups on the PAA chains, enhancing the composite system's mechanical property and stability. As the exchange progresses, the network undergoes microscopic reorganization and equilibrium restructuring, leading to the uniform dispersion of functional ions within the three-dimensional (3D) PAA framework. Accompanying this transformation, the hydrogel gradually changes from its initial transparent state (PAA) to a light green color (PFGH) (Fig. S1 in the ESM), finally forming a thermoelectric PFGH.

To elucidate the working principle of PFGH's thermoelectric performance, we illustrate the thermoelectric conversion process in Fig. 1(d), which is primarily governed by the thermodynamic differences of the $[Fe(CN)6]^{3-/4-}$ redox couple. At the hot end (anode), $[Fe(CN)_6]^{4-}$ undergoes oxidation ($[Fe(CN)_6]^{4-} \rightarrow e^- + [Fe(CN)_6]^{3-}$), releasing electrons to the external circuit. At the cold end (cathode), $[Fe(CN)_6]^{3-}$ is reduced back to $[Fe(CN)_6]^{4-}$ by accepting electrons ($[Fe(CN)_6]^{3-} + e^- \rightarrow [Fe(CN)_6]^{4-}$). This continuous redox cycling establishes a stable voltage between the two electrodes, enabling sustained thermoelectric conversion [14, 45]. The underlying driving force for this process stems from the thermodynamic differences between $[Fe(CN)_6]^{4-}$ and $[Fe(CN)_6]^{3-}$. Because $[Fe(CN)_6]^{4-}$ carries a higher negative charge density, it attracts more water molecules around it, forming a tightly bound and highly ordered hydration shell. This ordered structure results in lower thermodynamic entropy. At the hot end, the oxidation of $[Fe(CN)_6]^{4-}$ to $[Fe(CN)_6]^{3-}$ disrupts this compact hydration structure, releasing the constrained water molecules and increasing entropy. Since entropy increase is thermodynamically favorable at elevated temperatures, the oxidation reaction preferentially occurs at the hot end. As a result, this process continuously consumes $[Fe(CN)_6]^{4-}$ and generates $[Fe(CN)_6]^{3-}$ while lowering the electrode potential at the hot end. Conversely, at the cold end, the reduction of $[Fe(CN)_6]^{3-}$ back to $[Fe(CN)_6]^{4-}$ releases electrons and raises the electrode potential, thereby establishing a persistent potential difference between the two electrodes. The continuous redox reactions at different temperature regions create a concentration gradient that drives directional ion transport. The $[Fe(CN)_6]^{3-}$ generated at the hot end migrates toward the cold end through diffusion, convection, and electromigration, while $[Fe(CN)6]^{4-}$ flows toward the hot end for replenishment. Meanwhile, cations including K^+ and Gdm^+ migrate alongside the $[Fe(CN)6]^{3-/4-}$ species to maintain overall charge balance in the electrolyte.

To further enhance the hydrogel's thermoelectric performance, we introduced GdmCl to form thermosensitive crystals with

$[Fe(CN)_6]^{4-}$ [46]. As guanidinium salts rank at the top of the Hofmeister chaotropic series, Gdm^+ exhibits strong capability for disrupting non-covalent bonds. This enables Gdm^+ to preferentially aggregate around the high-charge-density $[Fe(CN)_6]^{4-}$, forming competitive coordination that reconstructs its solvation environment and disrupts the hydration shell's ordered structure. Notably, $[Fe(CN)_6]^{3-}$ remains minimally affected, and this selective interaction significantly amplifies the thermodynamic entropy difference between the two ions (Fig. 1(e)), effectively increasing the hydrogel's thermopower [47]. Additionally, the temperature-responsive behavior of crystal precipitation at the cold end and dissolution at the hot end further increases the migration rate difference between the $[Fe(CN)_6]^{3-/4-}$ redox pairs, leading to additional enhancement of PFGH's thermoelectric properties [48].

The morphological characteristics of freeze-dried hydrogels were analyzed through SEM. It should be noted that the porous structures observed in SEM images result from ice crystal formation during the freeze-drying process and may not precisely represent the microstructure of hydrogels in their hydrated state. As depicted in Fig. 1(f)(i), the freeze-dried MBA-crosslinked PAA hydrogel displays a porous network structure. After incorporating $[Fe(CN)_6]^{3-/4-}$ electrolyte, the freeze-dried PFH exhibits similar porous characteristics (Fig. S2 in the ESM).

Elemental mapping presented in Fig. S3 in the ESM confirms the uniform distribution of $[Fe(CN)_6]^{3-/4-}$ within the 3D network of the PAA hydrogel. The further introduction of GdmCl to construct the PFGH resulted in the formation of thermosensitive crystals. As shown in Fig. 1(f)(ii), Gdm^+ selectively induces $[Fe(CN)_6]^{4-}$ to form crystal particles with an average diameter of 0.8 μm (size distribution is shown in Fig. S4 in the ESM). These crystal particles are genuine structures formed during hydrogel preparation through the selective interaction between Gdm^+ and $[Fe(CN)_6]^{4-}$, and their formation is independent of the freeze-drying process. The magnified SEM view clearly reveals these crystal particles dispersed throughout the freeze-dried sample, directly validating our proposed thermoelectric enhancement mechanism based on thermosensitive crystallization. The extensive formation and dense distribution of these crystal particles lead to reduced visibility of the porous network in PFGH compared to PAA and PFH, as the crystals physically occupy and fill the pore space within the freeze-dried matrix. As shown in Fig. S5 in the ESM, the elemental mapping indicates a uniform distribution of K, Fe, N, and Cl elements, confirming the successful coexistence of $[Fe(CN)_6]^{3-/4-}$ and GdmCl within the hydrogel matrix.

Based on the working principle of the PFGH thermoelectric hydrogel system, we optimized key preparation parameters, including the concentration, type, and duration of the soaking solution, to obtain high-performance samples. The thermopower served as the primary performance metric during the optimization process, with measurements conducted using the experimental platform shown in Fig. S6 in the ESM. Firstly, we explored the effect of electrolyte concentration on performance. The concentration optimization reveals a non-monotonic relationship between $[Fe(CN)_6]^{3-/4-}$ concentration (0.1–0.4 M) and thermoelectric performance, with 0.3 M achieving a peak S of 1.2 $mV \cdot K^{-1}$ (Fig. 2(a)). Due to the higher charge density of $[Fe(CN)_6]^{4-}$, it forms a more compact hydration shell, resulting in lower thermodynamic entropy compared to $[Fe(CN)_6]^{3-}$. Below 0.3 M $[Fe(CN)_6]^{3-/4-}$, increasing concentration enhances the system's total entropy difference, leading to an increase in the S of PFH. However, when the concentration of $[Fe(CN)_6]^{3-/4-}$ exceeds 0.3 M, the interaction regions of individual $[Fe(CN)_6]^{3-/4-}$ begin to overlap with adjacent regions, resulting in a decrease in the thermodynamic entropy difference between $[Fe(CN)_6]^{4-}$ and $[Fe(CN)_6]^{3-}$, thus causing a reduction in the S of PFH [26].

Gdm^+ was introduced into the $[Fe(CN)_6]^{3-/4-}$ electrolyte solution to induce the formation of thermosensitive crystals between $[Fe(CN)_6]^{4-}$ and Gdm^+. This process enhanced the entropy difference of the $[Fe(CN)_6]^{3-/4-}$ redox couple, thereby improving the thermoelectric performance of the hydrogel. As shown in Fig. 2(b), when the concentration of $[Fe(CN)_6]^{3-/4-}$ ion pairs is maintained at 0.3 M, the S of PFGH initially rises and then decreases with the increase in GdmCl concentration from 0.5 to 2 M. This trend occurs because an optimal amount of GdmCl promotes thermosensitive crystal formation, increasing the entropy difference of $[Fe(CN)_6]^{3-/4-}$, whereas excessive GdmCl leads to over-crystallization. The latter reduces the concentration of free $[Fe(CN)_6]^{4-}$ in the solution, weakening the oxidation reaction. At 1.5 M GdmCl, PFGH achieves a peak S of 3.76 $mV \cdot K^{-1}$, which is 313% higher than that of PFH (0.3 M $[Fe(CN)_6]^{3-/4-}$ alone). This result underscores the effectiveness of Gdm^+ in promoting thermosensitive crystallization for thermoelectric performance enhancement. The resistance of PFGH was characterized using electrochemical impedance spectroscopy (EIS), and the conductivity (σ) was derived from equivalent circuit fitting (Fig. 2(c)). Similar to S, the σ of PFGH exhibits a non-monotonic dependence on GdmCl concentration, peaking at 1.39 $S \cdot m^{-1}$ for the 0.3 M $[Fe(CN)_6]^{3-/4-}$ and 1.5 M GdmCl system. This optimization arises because Gdm^+ partially shields the negative charge of $[Fe(CN)_6]^{4-}$ via electrostatic interactions, reducing interionic Coulombic repulsion and enhancing electron transfer efficiency. However, at higher Gdm^+ concentrations, excessive thermosensitive crystal formation impedes ion mobility, thereby degrading σ [45].

To systematically optimize the electrolyte system, we maintained a fixed molar ratio of $[Fe(CN)_6]^{3-/4-}$ to GdmCl at 1:5 while simultaneously adjusting their concentrations. As shown in Fig. S7 in the ESM, both the S and σ (derived from the EIS analysis in Fig. S8 in the ESM) of PFGH increase with higher total ion concentrations. This enhancement can be attributed to an increased charge carrier density between the electrodes. Additionally, the thermoelectric performance was further evaluated through power factor (PF = $S^2 \cdot \sigma$) analysis. As shown in Fig. 2(d), the optimal composition of 0.3 M $[Fe(CN)_6]^{3-/4-}$ and 1.5 M GdmCl yields the highest PF value of 18.5 $\mu W \cdot m^{-1} \cdot K^{-2}$, establishing this formulation as the preferred choice for subsequent investigations. We then examined the influence of soaking time on PFGH performance using the optimized electrolyte solution. Figure 2(e) reveals that PFGH soaked at 60 °C for 1 h exhibited peak thermoelectric performance. Notably, prolonged soaking leads to performance degradation, which can be attributed to the acidic environment (pH decreasing from 6 to 3.5 within 0.5 h, Fig. S9 in the ESM) due to PAA hydrogel dissolution. Under these acidic conditions combined with elevated temperature (60 °C), GdmCl decomposes into organic byproducts that compromise system efficiency. The electrochemical characterization of PFGH (Fig. 2(f)) reveals reversible redox behavior, featuring distinct oxidation and reduction peaks at +0.4 and −0.4 V, respectively. The complete overlap of these redox peaks over three consecutive scans confirms the excellent reaction reversibility and the stability of the hydrogel.

Soaking the PAA hydrogel in a $[Fe(CN)_6]^{3-/4-}$-GdmCl solution

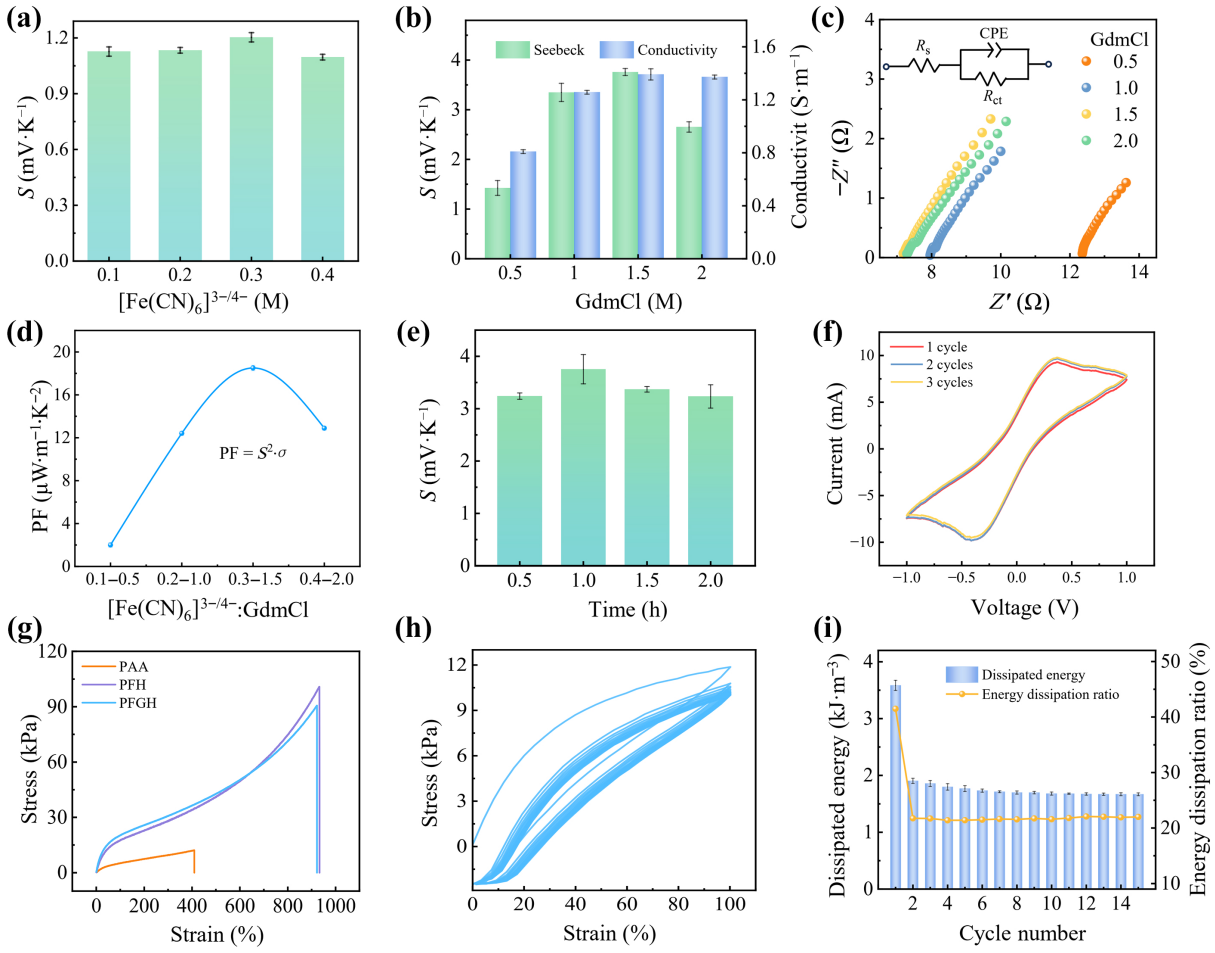

Figure 2 Exploration on thermoelectric and mechanical properties of PFGH. (a) *S* of PFH soaking in different $[Fe(CN)_6]^{3-/4-}$ solutions. (b) *S* and conductivity of PFGH soaking in 0.3 M $[Fe(CN)_6]^{3-/4-}$ and different GdmCl mixed solutions. (c) Electrochemical impedance spectroscopy of PFGH soaking in 0.3 M $[Fe(CN)_6]^{3-/4-}$ and different GdmCl mixed solutions (inset shows the equivalent circuit diagram). (d) PF of PFGH soaking in *x* M $[Fe(CN)_6]^{3-/4-}$-*y* M GdmCl mixed solutions (*x*:*y* =1:5). (e) *S* of PFGH as a function of soaking time. (f) Three-cycle CV curves of PFGH. (g) Stress–strain curves of PAA, PFH, and PFGH. (h) 15-cycle loading-unloading curves of PFGH under a strain of 100%. (i) Dissipated energy and energy loss ratio per cycle for (h).

not only enhanced the thermoelectric performance of the PFGH but also significantly improved its mechanical properties, including toughness and strength. The stress–strain tests (Fig. 2(g)) reveal that after incorporating $[Fe(CN)_6]^{3-/4-}$, PFH exhibits a dramatic increase in tensile strength (from 12 to 90 kPa) and an elongation at break (from 409% to 920%), with tensile testing images provided in Fig. S10 in the ESM. The mechanical properties of PFGH are equivalent to those of PFH upon the introduction of Gdm^+, suggesting that the reinforcement primarily stems from the hydrogen bonding network between $[Fe(CN)_6]^{3-/4-}$ and the PAA framework. To investigate these hydrogen bonding interactions, we conducted FTIR spectroscopy. The spectrum of pure PAA exhibits a characteristic –OH stretching peak at ~ 3342 cm^{-1} (Fig. S11 in the ESM). Upon the addition of $[Fe(CN)_6]^{3-/4-}$, this peak undergoes a red shift to 3353 cm^{-1} in PFH, indicating strong hydrogen bonding between $[Fe(CN)_6]^{3-/4-}$ and the PAA hydrogel. In contrast, while Gdm^+ and PAA form hydrogen bonds, PFGH only displays a slight red shift. This similarity results in PFH and PFGH exhibiting comparable mechanical properties. A schematic of the proposed hydrogen bonding network is illustrated in Fig. S12 in the ESM. Further analysis reveals that PFGH's elastic modulus increases from 2.38 to 5.36 kPa, and its toughness enhances from 9.30 to 42.4 $kJ·m^{-3}$ (Fig. S13 in the ESM), achieving simultaneous improvements in both strength and toughness. To highlight these enhancements, PFGH was subjected to bending, twisting, and stretching tests, as well as load-bearing trials with 100 g weights, all confirming its exceptional flexibility and robustness (Fig. S14 in the ESM). The fatigue resistance of PFGH, which is crucial in practical applications, was assessed through 15 cyclic tensile tests at 100% strain (Fig. 2(h)). The initial cycle displays a pronounced hysteresis loop with an energy dissipation of 3.5 $kJ·m^{-3}$ (Fig. 2(i)), attributed to molecular chain rearrangement and reversible non-covalent bonding. In subsequent cycles, the hysteresis loops decrease, with the energy dissipation and loss rates stabilizing at 1.6 $kJ·m^{-3}$ and 26% by the 15th cycle, respectively, indicating excellent fatigue resistance and structural stability of PFGH.

The exceptional thermoelectric and mechanical properties of PFGH contribute to its outstanding performance in temperature sensing, thermal energy harvesting, and self-powered strain sensing applications. As illustrated in Fig. 3(a), the temperature sensing capability of PFGH was first investigated, and the relationship between the thermoelectric voltage and temperature difference ($\Delta T = T_h - T_c$) exhibits good linearity within a range of 10 K. The calculated *S* of 3.76 $mV·K^{-1}$ confirms that PFGH possesses high temperature detection sensitivity. To further characterize its temperature response characteristics, PFGH was tested under

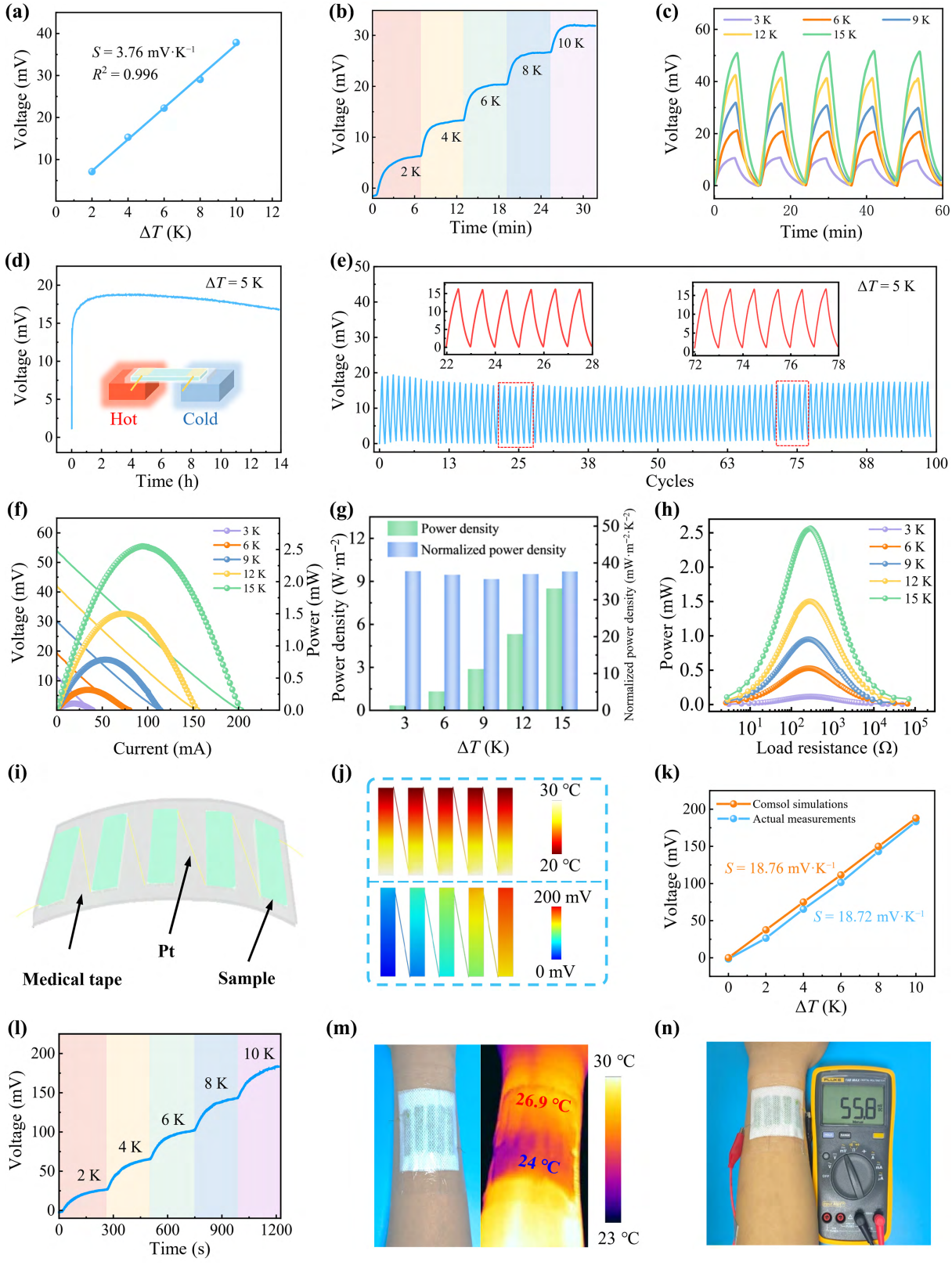

Figure 3 Thermoelectric performance test of PFGH. (a) Output voltage vs. ΔT for PFGH. (b) Continuous output voltage variation of PFGH under increasing ΔT. (c) Cyclic response of PFGH under different ΔT. ((d) and (e)) Long-term output capability and cycling stability under ΔT of 5 K. (f) Output power test of PFGH under different ΔT. (g) Maximum output power density and specific power density. (h) Output power vs. load resistance of PFGH under different ΔT. (i) Schematic diagram of thermoelectric device array assembly. (j) Temperature and electric potential field distribution of PFGH array simulated by COMSOL. (k) Comparison between experimental measurement and COMSOL simulation of the relationship that output voltage vs. ΔT of PFGH array. (l) Continuous output voltage variation of PFGH array under increasing ΔT. ((m) and (n)) Infrared images of the PFGH array fixed on an arm (one end contacting skin, and the other insulated) and its output voltage.

increasing temperature gradient and cyclic temperature difference, respectively. As shown in Fig. 3(b), the output voltage of PFGH exhibits synchronous growth with rising ΔT, demonstrating precise recognition and stable sensing performance. Notably, PFGH achieves an ultrahigh temperature resolution with a minimum detectable ΔT of 0.1 K (Fig. S15 in the ESM). With periodic fluctuations in ΔT, the output voltage of PFGH exhibits highly corresponding regular changes, indicating that PFGH can accurately capture and respond to environmental temperature variations (Fig. 3(c)). This behavior confirms PFGH's ability to accurately monitor environmental temperature changes while maintaining excellent signal reproducibility, laying a solid foundation for subsequent temperature sensing and self-powered energy supply applications. To assess operational stability, PFGH was subjected to a 14-h continuous test at a constant ΔT of 5 K (Fig. 3(d)). The results indicate exceptional long-term stability and small performance degradation. Additionally, after 100 cycles at ΔT of 5 K, PFGH maintains stable voltage output, demonstrating remarkable durability suitable for practical implementations (Fig. 3(e)).

Furthermore, the thermoelectric power generation performance of PFGH was evaluated under varying ΔT. As depicted in Fig. 3(f), both the open-circuit voltage (V_{oc}) and the maximum output power (P_{max}) increase with rising ΔT. When the ΔT was 15 K, the V_{oc} and P_{max} values of PFGH were 54 mV and 2.55 mW, respectively, significantly surpassing those of conventional electronic thermoelectric devices. For comprehensive performance evaluation, we introduced two key metrics of power density (P_d) and temperature-normalized power density ($P_d/\Delta T^2$). Figure 3(g) demonstrates that the maximum output power density increases with increasing ΔT, peaking 8.50 $W \cdot m^{-2}$ when ΔT reaches 15 K. After normalization by ΔT^2, PFGH exhibits a consistent normalized power density of 37.77 $mW \cdot m^{-2} \cdot K^{-2}$, providing a standardized measure of its thermoelectric capability. To investigate the load-matching characteristics of PFGH, we conducted systematic load testing experiments. The output voltage measurement (Fig. S16 in the ESM) demonstrates that under ΔT of 6 K, the output voltage tended to stabilize when the external load resistance exceeded 10 kΩ, reaching a maximum voltage of 19.4 mV at 65 kΩ. The output power test results indicate that the PFGH achieves its maximum power output at a load resistance of 267 Ω (Fig. 3(h)), offering essential guidance for circuit design and impedance matching in practical applications.

To enhance the output voltage and power of hydrogel devices to meet practical application requirements, a PFGH array composed of five PFGH cells in series was designed and fabricated (Fig. 3(i)). COMSOL finite element simulation was used to simulate the temperature field and potential distribution of PFGH array. As shown in Fig. 3(j), the temperature field of the PFGH array exhibits uniform distribution, whereas the electric potential distribution progressively increases across the five cells, reaching 187.94 mV at a ΔT of 10 K. Finite element simulation of PFGH array at other ΔT (2–8 K) is presented in Fig. S17 in the ESM. The output voltage of the PFGH array was measured across a range of ΔT (2–10 K). Figure 3(k) shows a good agreement between experimental measurements and finite element simulations, with the array exhibiting a notable S of 18.72 $mV \cdot K^{-1}$. Figure 3(l) shows that the output voltage of the PFGH array increases synchronously with increasing ΔT (2–10 K), indicating the PFGH array's precise temperature recognition and signal stability. For wearable applications, we evaluated the mechanical robustness of the array through bending tests. The bending cycles test induces minimal relative resistance variation ($\Delta R/R_0$ < 10%, Fig. S18(a) in the ESM), while maintaining stable thermoelectric output at ΔT of 5 K (Fig. S18(b) in the ESM), showcasing reliable performance under deformation. Based on the excellent thermoelectric performance and mechanical stability of the PFGH array, its practical application was demonstrated through body heat harvesting. The PFGH array was attached to the human arm, with one end contacting with the skin as the hot end, and the other end contacting the thermal insulation layer on the skin surface as the cold end. The test results show that the PFGH array builds ΔT of 3 K on the arm surface (Fig. 3(m)) and generates an output voltage of 55.8 mV (Fig. 3(n)), highlighting the efficient conversion of body heat into usable electrical energy by the PFGH array.

Owing to its stable thermoelectric performance, exceptional mechanical properties, and superior electrical characteristics, PFGH exhibits significant potential for self-powered strain sensing applications. Strain sensing behavior of PFGH was characterized and is shown in Fig. 4(a), demonstrating that the $\Delta R/R_0$ of PFGH exhibits a linear dependence on strain, featuring an impressive working range that extends up to 920%. The strain sensitivity, quantified by the gauge factor (GF), displays a three-stage linear response of 0.54 (strain of 0%–200%), 1.11 (200%–600%), and 1.70 (600%–920%), respectively. Cyclic stability tests further confirmed the reliability of PFGH under varying strain amplitudes. Figure S19 in the ESM illustrates consistent and reproducible output signals across five cycles, encompassing both small (10%–50%) and large (100%–500%) strain ranges, thereby emphasizing its robust performance for dynamic sensing applications. As illustrated in Fig. 4(b), the $\Delta R/R_0$ curves during both incremental and decremental stepwise strain (0%–100%) exhibit negligible hysteresis or signal attenuation, demonstrating the exceptional static response stability of PFGH. Additionally, the average response and recovery time for PFGH strain sensing were both 180 ms (Fig. 4(c)), enabling swift force-to-electrical signal conversion. Furthermore, the impact of strain rate on sensing performance was investigated. Figure S20 in the ESM verifies that PFGH maintains precise signal conversion across various stretching rates (100–400 $mm \cdot min^{-1}$), ensuring reliable detection under different motion speeds.

Leveraging PFGH's outstanding thermoelectric conversion capabilities and superior strain sensing attributes, we engineered a self-powered strain sensing system. The fundamental working mechanism is depicted in Fig. 4(d). When subjected to a temperature gradient, PFGH generates an initial current (I_0) through reversible redox reactions of $[Fe(CN)_6]^{3-/4-}$ ion pair. For a fixed-resistance PFGH, I_0 has a linear relationship with the applied ΔT, facilitating temperature monitoring via current measurement. Furthermore, mechanical deformation alters the internal resistance of PFGH, thereby modulating its output current. By tracking the relative current change ($\Delta I/I_0$), strain can be quantitatively assessed. A key advantage of this design is that the electric signal generated by ΔT serves not only as a temperature indicator but also as an intrinsic power source for strain sensing, thereby achieving the self-powered strain sensing functionality.

To validate the self-powered sensing capabilities of PFGH, we devised an experimental setup (Fig. 4(e)) that integrates Peltier devices (for imposing ΔT) with a universal testing machine (for applying strain). Thermocouples continuously monitored the real-time sample temperatures. Under a constant ΔT, PFGH's

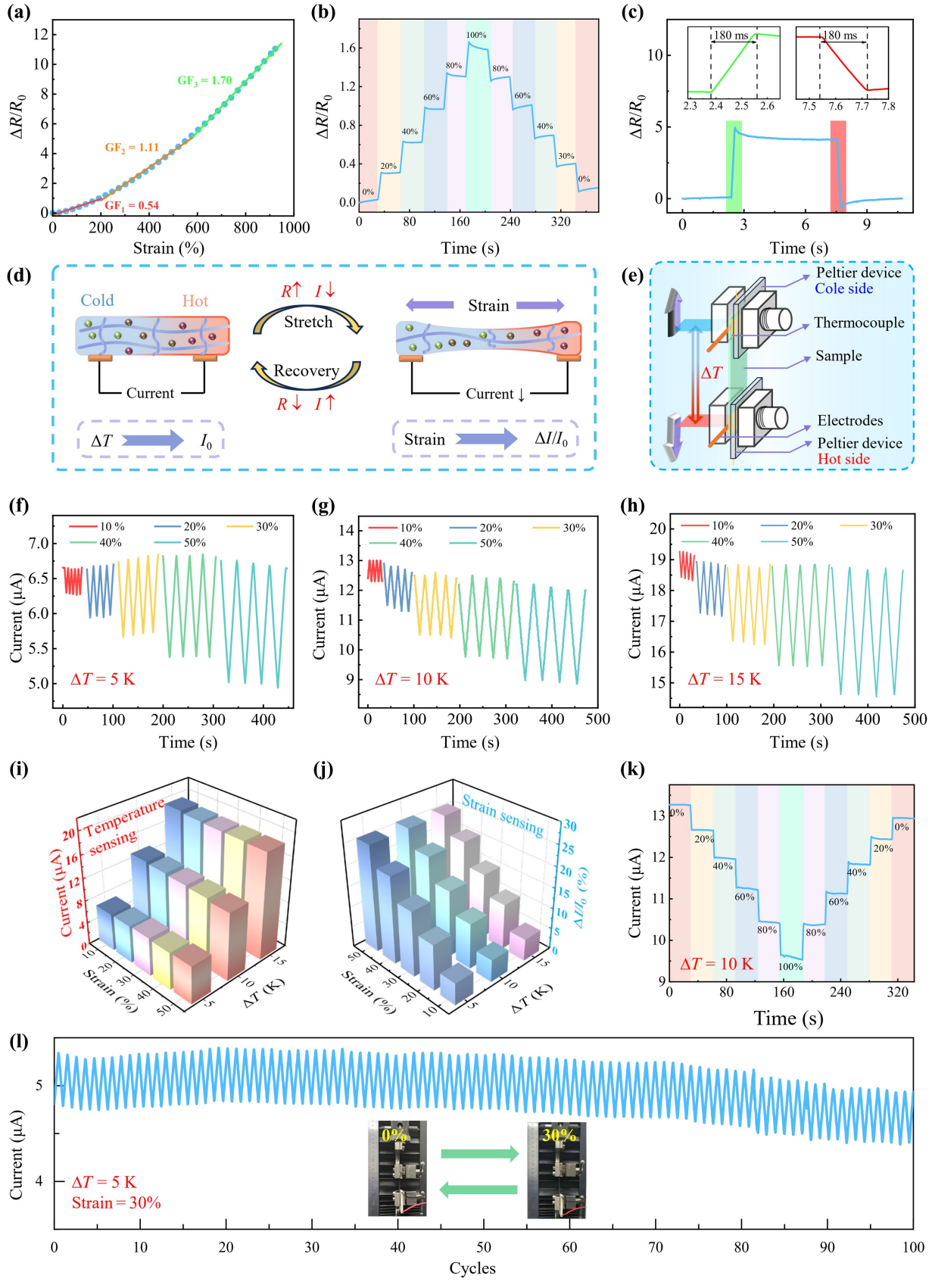

Figure 4 The sensing performance test of PFGH. (a) $\Delta R/R_0$ of PFGH under different strains. (b) $\Delta R/R_0$ of PFGH under stepwise strain. (c) Response and recovery time of PFGH. ((d) and (e)) Mechanism diagram and testing schematic of self-powered strain sensing. ((f)–(h)) Current changes of PFGH under different strains at ΔT of 5, 10, and 15 K. (i) Initial current changes and (j) relative current changes of PFGH, which are respectively used for temperature sensing and strain sensing. (k) Self-powered sensing of PFGH under step strain. (l) 100-cycle stability test of PFGHs self-powered sensing.

thermoelectric current exhibits a predictable decrease as the strain increased (Figs. 4(f)–4(h)), whereas the I_0 remains largely stable across diverse strain states. Given typical human skin deformation ranges (< 50%), we focused on strains of 10%–50%. To comprehensively assess the self-powered strain sensing capability of PFGH, the current changes of PFGH under varying ΔT and strain conditions were meticulously analyzed. As shown in Fig. 4(i), the I_0 of PFGH increases linearly with rising ΔT (5, 10, and 15 K), yet it remains stable across different strain levels, indicating that the I_0 is directly proportional to the ΔT values and is insensitive to variations in strain magnitude. Meanwhile, Fig. 4(j) reveals that the $\Delta I/I_0$ maintains exceptional consistency with applied strain (10%–50%) regardless of the ΔT, confirming the capability of PFGH for accurate strain detection through current variations, without interference from external temperature fluctuations. Notably, since the measured current signal originates from PFGH's thermoelectric properties rather than external power sources, this sensing mechanism qualifies as self-powered strain detection. To assess the stability of PFGH's self-powered sensing performance, the sensing characteristics under various conditions were systematically examined. As depicted in Fig. S21 in the ESM, PFGH exhibits minimal fluctuation in thermoelectric current signals across a broad strain rate range of 100–400 mm·min^{-1}, thereby confirming the system's low susceptibility to strain rate variations. Additionally, PFGH demonstrates exceptional current response stability under stepwise strain loading from 0% to 100% (Fig. 4(k)), underscoring its superior strain tracking capability. To evaluate the long-term performance stability, 100 cyclic tensile tests were conducted under conditions of ΔT of 5 K and strain of 30%. The results (Fig. 4(l)) reveal that PFGH maintains consistent signal stability and reliability. These findings collectively highlight PFGH's exceptional self-powered sensing performance, laying a solid foundation for its application in human body thermal energy-based self-powered strain sensing systems.

Leveraging PFGH's exceptional temperature sensing performance and self-powered strain sensing capabilities, we explored its practical applications in wearable human motion and health monitoring. First, the non-contact temperature sensing functionality was investigated. As shown in Fig. 5(a), when the distance between PFGH and a constant-temperature Peltier device (50 °C) increases from 10 to 100 mm, the thermoelectric voltage decreases from 1.23 to 0.01 mV, accurately mapping the surrounding temperature field resulting from thermal radiation emitted by the heat source. To assess sensing stability, we conducted cyclic distance tests between PFGH and the heat source. The results, as depicted in Fig. 5(b), exhibit highly reproducible and stable voltage signals at varying distances (10, 15, and 20 mm). Furthermore, we integrated PFGH onto a finger for non-contact distance detection of a heat source. As the finger moves closer to the heat source in a stepwise manner (Fig. 5(c)), the thermoelectric voltage of PFGH increases progressively, thereby confirming its potential for non-contact thermal monitoring. This capability unlocks new avenues for applications such as environmental temperature mapping and the protection of thermal-sensitive equipment. Continuous monitoring of respiratory status across various motion states facilitates real-time assessment of human health conditions. Leveraging the temperature-sensing capabilities of PFGH, we developed a self-powered respiratory monitoring system to evaluate breathing patterns under differing exercise intensities. As depicted in Fig. 5(d), the PFGH device is seamlessly integrated into a mask, forming a dynamic respiratory monitoring system. The cold end of the PFGH functions as a temperature reference by contacting ambient air, whereas the hot end, positioned near the upper lip, serves as the detection terminal. This system converts breathing-induced temperature fluctuations into quantifiable voltage signals, enabling passive monitoring. Through infrared thermal imaging (Fig. 5(e)), we distinctly observed dynamic temperature variations during respiration, thereby validating the system's feasibility. This temperature difference-based detection mechanism presents a novel technical approach for passive respiratory monitoring. To systematically assess the system's adaptability across varying physical activity levels, we performed comparative testing under four representative motion states: sitting, walking, squatting, and running (Figs. 5(f)–5(i)). The results reveal that the device's thermoelectric output exhibited periodic voltage fluctuations synchronized with respiratory cycles. Additionally, the amplitude variations in voltage consistently correlates with exercise intensities across different activities, highlighting the system's precise capability in detecting respiratory rhythms. Beyond non-contact temperature sensing and respiratory monitoring, PFGH also exhibits substantial potential for self-powered wearable sensing applications. As depicted in Fig. 5(j), PFGH sensors were affixed to human joints to monitor body movements by harnessing human thermal energy. The magnified view in Fig. 5(j) details the PFGH sensor, with one end contacting the skin as the heat source and the other end connected to a thermally insulating material as the cold end. This configuration leverages the temperature difference between the body and the environment to generate current signals, thereby enabling self-powered motion monitoring. Initial tests on finger joints (Fig. 5(k)) revealed that the output current of PFGH increased proportionally with bending angles (ranging from 45° to 90°), showcasing precise motion detection capabilities. Notably, the current variations exhibit exceptional consistency during repetitive movements at fixed angles, affirming the reliability of PFGH in fine motion recognition. For larger movements, PFGH accurately tracked electrical signal changes throughout the full range of elbow flexion (Fig. 5(l)). Applications involving multiple joints (neck, wrist, and knee) demonstrate excellent stability and reproducibility (Fig. 5(m)), further substantiating the broad adaptability of PFGH. These capabilities render it particularly invaluable for driver safety monitoring (tracking neck movements) and for sports rehabilitation as well as elderly mobility assessment (analyzing wrist and knee joints).

PFGH demonstrates exceptional thermoelectric capabilities, exhibiting both stable voltage generation and polarity-dependent (positive or negative) output that correlates directly with temperature gradient direction. The experimental results in Fig. S22 in the ESM clearly show this characteristic, where PFGH arrays generate +220 and −87 mV when contacted to 33 °C warm water and 14 °C cool water respectively, confirming its accurate temperature gradient discrimination. Based on this temperature sensitive behavior, an intelligent cold/hot response switch system was developed. This device integrates three key functional components: the PFGH thermoelectric module, a voltage amplification circuit, and a bidirectional light-emitting diodes (LEDs) indicator system with yellow and blue diodes connected in antiparallel configuration. The system's visual monitoring of environmental cold and hot temperature changes are visually demonstrated in Fig. 6(a) through three distinct states. As shown in Fig. 6(a)(i), when the system contacts human body temperature of

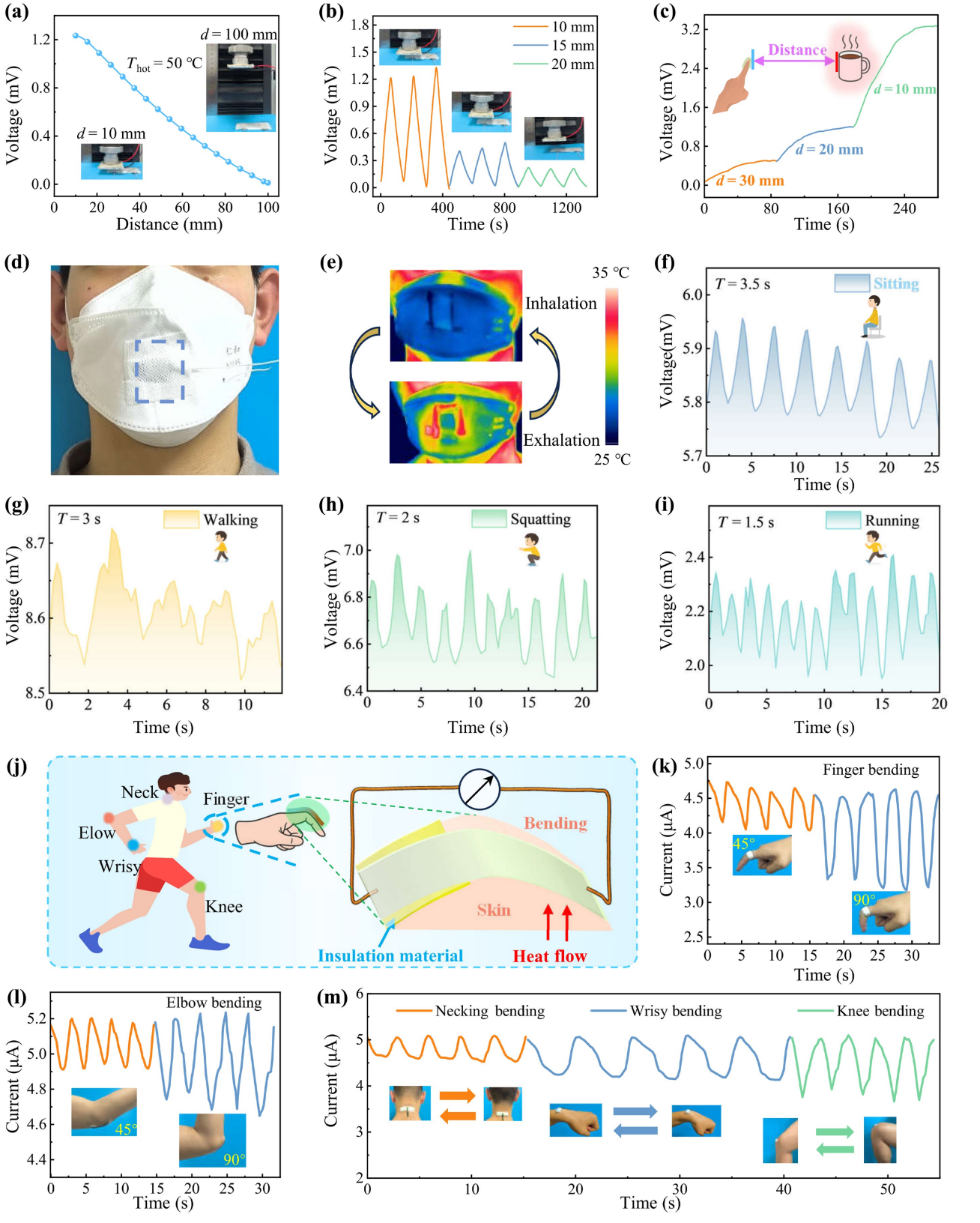

Figure 5 Self-powered temperature sensing application based on PFGH. (a) Voltage response signal of PFGH with varying heat source distance. (b) Cyclic voltage response of PFGH with different heat source distances. (c) Non-contact temperature sensing application. (d) Photograph of a mask embedded with the PFGH device (cold end exposed to air and the hot end positioned near the upper lip). (e) Infrared thermal images of the mask during inhalation and exhalation, demonstrating temperature variation. ((f)–(i)) Real-time respiratory frequency monitoring using the PFGH-integrated mask under different physical states (sitting, walking, squatting, and running). (j) Schematic diagram of PFGH devices attached to various body parts for self-powered motion sensing, utilizing human body thermal energy. ((k)–(m)) PFGH for self-powered detecting joint movements of fingers, elbows, neck, wrists, and knees.

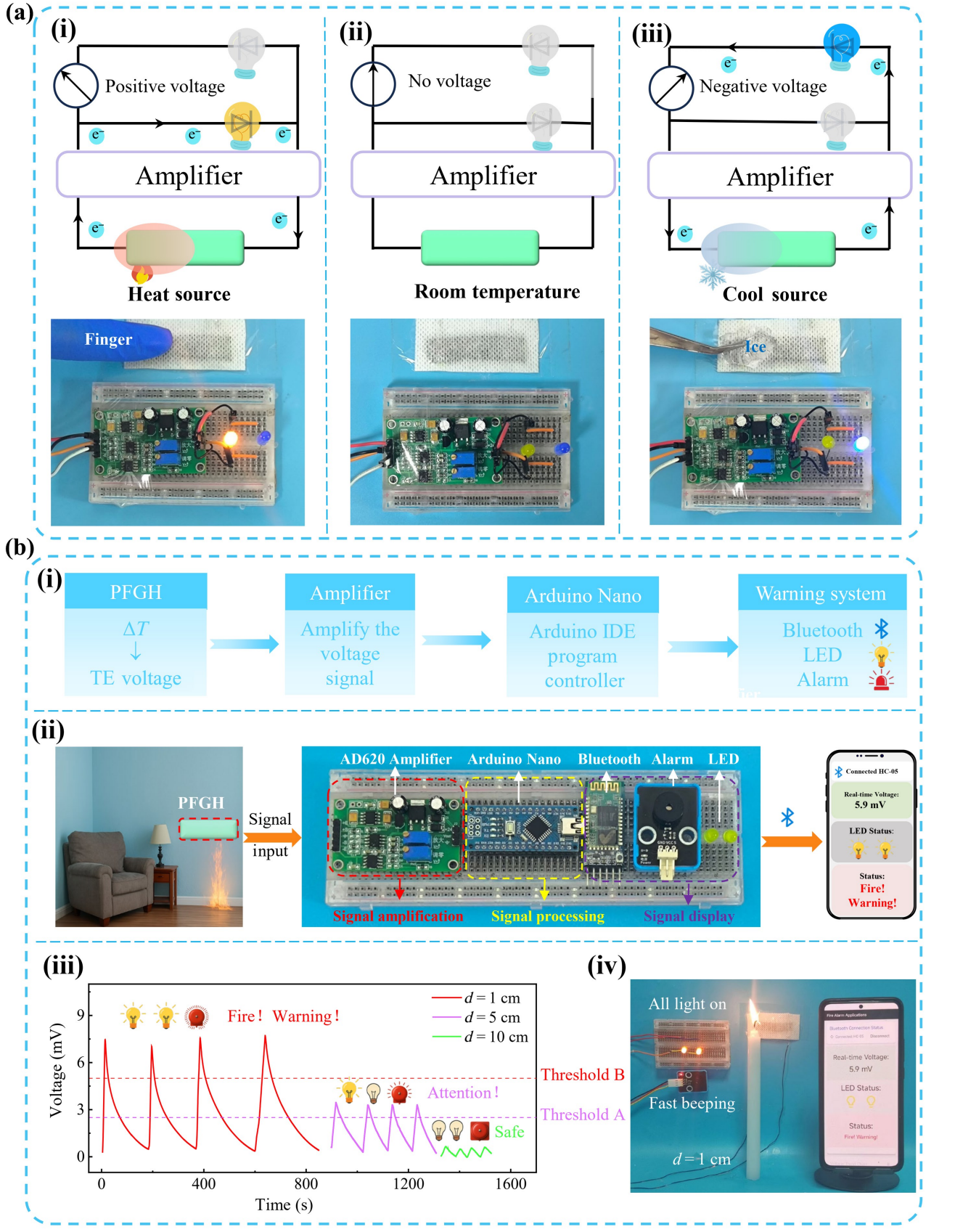

Figure 6 Intelligent cold/hot response switch system and fire warning system based on PFGH. (a) Schematic diagram and demonstration of PFGH temperature indicator: (i) yellow light activation upon finger contact, (ii) no response at room temperature, and (iii) blue light triggering when contacted to ice. (b) PFGH fire alarm application: (i) fire alarm mechanism diagram, (ii) fire alarm system composition and mobile APP interface, (iii) voltage signals at different fire source distances and corresponding states of light, buzzer, and mobile interface, and (iv) full system activation (light, buzzer, and APP alerts) when fire source is 1 cm from PFGH.

approximately 33 °C, PFGH generates a positive voltage, activating the yellow LED after signal amplification. The ambient conditions maintain the system in a dormant state, with no voltage output and inactive indicators (Fig. 6(a)(ii)). As depicted in Fig. 6(a)(iii), when the testing end of PFGH comes into contact with a low-temperature object, such as ice, it generates a negative voltage that causes the blue LED to illuminate. This design facilitates real-time and visual temperature monitoring using different optical signaling, where each state corresponds to specific thermal conditions.

To further explore PFGH's potential in temperature detection applications, we developed an intelligent fire warning system with multi-level alert capabilities. As illustrated in Fig. 6(b)(i), the system architecture comprises three core components: (1) PFGH thermoelectric modules for temperature difference conversion, (2) AD620-based signal amplification circuits, and (3) Arduino Nano microcontrollers for data processing and logic control. This system supports a comprehensive warning network that integrates three parallel alert channels: visual LED indicators, audible buzzer alarms, and bluetooth-enabled mobile notifications. The operational mechanism of this warning system is illustrated in Fig. 6(b)(ii). The system continuously monitors environmental temperature through PFGH's thermoelectric conversion capability. When abnormal temperature increases are detected, the resulting thermal gradient generates corresponding voltage signals, which are then amplified and processed by the AD620 and microcontroller, respectively. Figure S23 in the ESM presents the data analysis and primary discrimination logic utilizing the Arduino platform, which implements a three-tier classification scheme based on predefined voltage thresholds: a safe state (< 2.5 mV), an attention state (2.5–5 mV), and a fire warning state (> 5 mV). Following this logical assessment, the system simultaneously transmits state-specific alarm information to all connected warning terminals. Experimental validation using candle flame simulations (Fig. 6(b)(iii)) demonstrates consistent performance across varying threat distances (1, 5, and 10 cm). Figure 6(b)(iv) illustrates the alarm responses of the intelligent fire warning system in simulated scenarios. At a critical proximity of 1 cm, the system triggers a maximum alert with dual LED activation, high-frequency buzzer tones, and "Fire! Warning!" mobile alerts. At an intermediate distance of 5 cm (Fig. S24(a) in the ESM), moderate warnings are activated (single LED, medium-frequency buzzer, and "Attention! " status on mobile devices). When the candle is 10 cm away from the PFGH (Fig. S24(b) in the ESM), the LED indicator remains off, the buzzer stays silent, and the mobile application displays a "Safe" status. The dynamic transition between these states is captured in Video S1 in the ESM, confirming the reliability of the intelligent fire warning system in fire detection scenarios through its multi-channel warning mechanism.

With the rapid advancement of machine learning in sensing applications, wearable devices are increasingly evolving toward intelligent functionality. This study developed an efficient material identification system based on PFGH devices by precisely capturing characteristic voltage signals generated during material interface heat transfer and integrating them with machine learning algorithms, enabling accurate classification of material types. Figure 7(a) depicts the fundamental operating principle of this identification system. When a heat source is applied to the base of a test material, various materials display unique surface temperatures because of their distinct thermal conduction properties. Upon contact with the material, the PFGH device detects the resulting temperature gradient and generates corresponding thermoelectric voltage signals. By extracting and analyzing these voltage signal features in conjunction with a random forest machine learning algorithm, the system achieves precise material identification. Six representative materials with varying thermal conductivity properties were selected for testing: aluminum (Al), glass, polyvinyl chloride (PVC), phenolic resin (PF), wood, and paper (Fig. 7(b)). Prior to experimental validation, finite element simulations were conducted using COMSOL software to analyze the heat transfer behavior of these materials, with detailed simulation parameters provided in Table S1 in the ESM. Figure 7(c) presents the simulated surface temperature distributions of the six materials under identical heating conditions. These theoretical predictions show strong agreement with the experimental observations presented in Fig. S25 in the ESM, establishing a robust foundation for material differentiation based on thermal conduction characteristics.

Using the experimental setup depicted in Fig. S26 in the ESM, we measured the thermoelectric voltage signals generated when the PFGH device contacted various materials, each backed by Peltier heating plates. As shown in Fig. 7(d), each test cycle consists of a 20-s contact phase followed by a 40-s recovery phase, revealing significant differences in both peak voltage amplitudes and dynamic signal characteristics across materials. Data analysis reveals a clear correlation between the thermal conductivity of materials and the magnitude of voltage response, with materials of higher conductivity producing proportionally greater signal amplitudes (Fig. 7(e)). These distinctive response patterns serve as critical input features for our machine learning model. To achieve machine learning identification, the random forest algorithm was adopted as the classification tool (Fig. 7(f)). The training process commences with extensive dataset collection, as depicted in Fig. 7(g), which illustrates representative voltage–time curves obtained through multiple sampling cycles. We partitioned the dataset into training (70%) and testing (30%) subsets, then constructed multiple decision trees, each independently trained through random selection of feature subsets and sample subsets. The system's output was determined by majority voting across all decision trees, ensuring robust material identification.

To evaluate the algorithm's classification performance, we employed *t*-distributed stochastic neighbor embedding (*t*-SNE) for dimensionality reduction to visualize the high-dimensional feature space in two-dimensions (Fig. 7(h)). This visualization clearly reveals the intrinsic data structure, with distinct color-coded clusters representing each of the six material categories. The results demonstrate strong intra-class cohesion and effective inter-class separation, confirming the system's discriminative capability. Quantitative evaluation using the confusion matrix (Fig. 7(i)) demonstrated exceptional classification performance, with the system achieving a 98.7% average accuracy across six material types. These results validate that the material identification method, which combines PFGH devices with machine learning, possesses excellent classification performance and application potential.

4 Conclusions

In conclusion, this work successfully develops a PAA-based thermoelectric hydrogel PFGH. By introducing GdmCl to induce $K_4Fe(CN)_6$ the formation of thermosensitive crystals, the entropy difference between the redox couple $[Fe(CN)_6]^{3-/4-}$ is effectively increased, thereby enhancing its thermoelectric performance. The

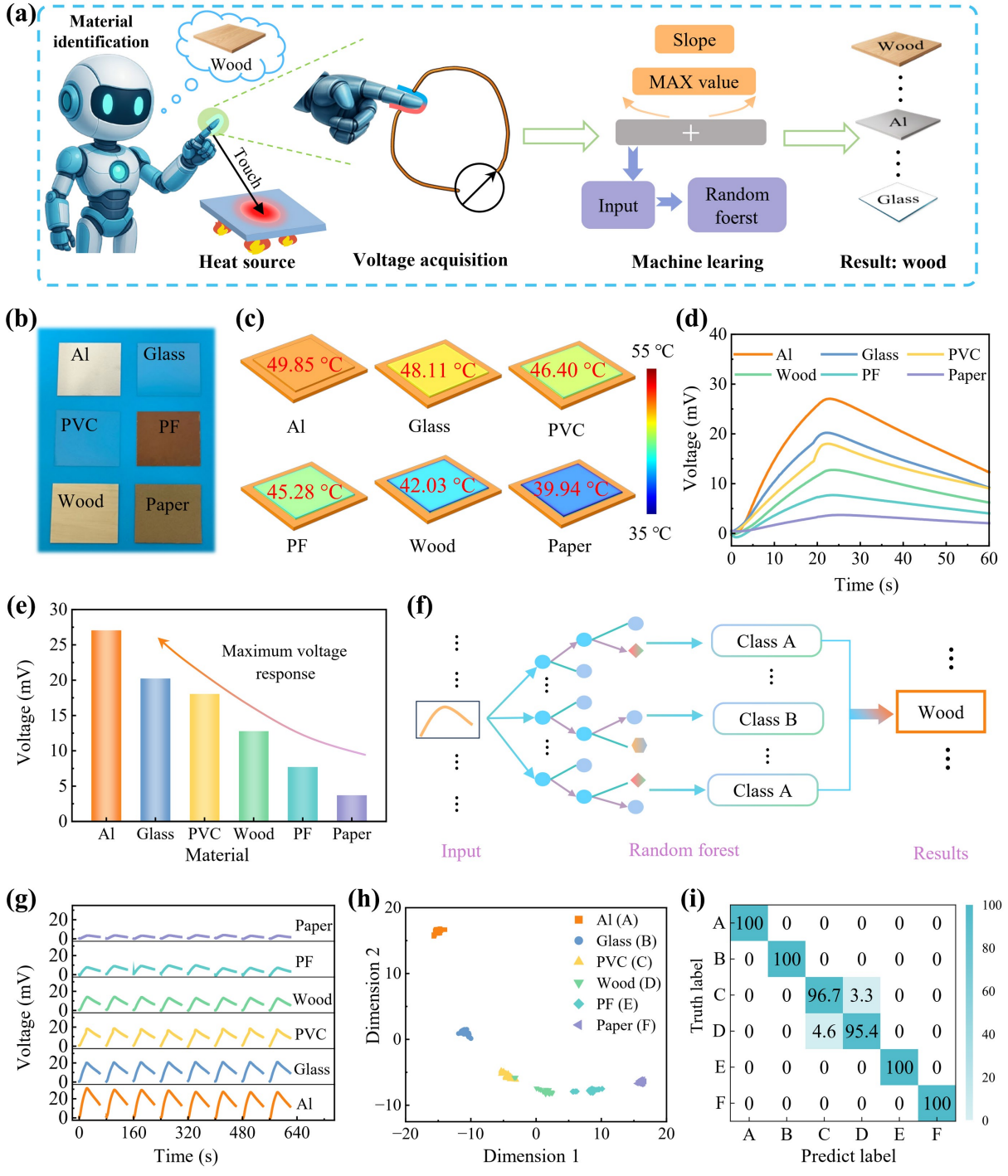

Figure 7 Machine learning-assisted material identification of PFGH. (a) Schematic diagram of machine learning-assisted material identification model using PFGH device. (b) Six test materials with different thermal properties and (c) their corresponding heat transfer simulation results. (d) The characteristic thermoelectric response curves recorded during 20-s contact with each material and (e) the maximum voltage values. (f) The random forest classification algorithm workflow. (g) Partial voltage cycling data of six materials. ((h) and (i)) Material clustering diagram and confusion matrix of six materials after machine learning training.

optimized PFGH achieves a thermopower of 3.56 mV·K^{-1} and a normalized output power density of 37.77 mW·m^{-2}·K^{-2} under the ratio of 0.3 M $[Fe(CN)_6]^{3-/4-}$ and 1.5 M GdmCl, while possessing excellent mechanical properties with a tensile strength of 90 kPa and an elongation at break of 920%. PFGH exhibits outstanding temperature sensing capabilities and self-powered strain sensing properties, facilitating applications such as temperature identification, respiratory monitoring, and self-powered motion detection in wearable devices. Furthermore, PFGH achieves multi-channel fire detection and reaches a material identification accuracy of 98.7% by integrating random forest algorithms with the differential heat transfer characteristics at material interfaces, showcasing its potential application in the field of intelligent sensing. This study advances the design of ionic thermoelectric materials and provides a scalable pathway for developing low-cost and high-performance self-powered sensors. The findings could

accelerate progress in wearable electronics and smart material recognition technologies.

Electronic Supplementary Material: Supplementary material (optical photographs and SEM images of PFGH, photographs of the thermoelectric performance testing apparatus, FTIR spectra of various samples, schematic illustration of hydrogen bonding networks in PFGH, optical photographs of the samples under various deformation modes, simulation of device thermoelectric performance and cyclic stability testing, cyclic response signals of the samples, flowchart of the fire alarm sensor, and infrared thermal imaging of heat transfer in different materials) is available in the online version of this article at https://doi.org/10.26599/NR.2026.94908553.

Data availability

All data needed to support the conclusions in the paper are presented in the manuscript and the Electronic Supplementary Material. Additional data related to this paper may be requested from the corresponding author upon request.

Acknowledgements

The authors gratefully acknowledge the financial support of this work by the National Natural Science Foundation of China (No. 52373093), Excellent Youth Fund of Natural Science Foundation of Henan Province (No. 242300421062), Central Plains Youth Top Notch Talent Program of Henan Province, Scientific and Technological Project in Henan Province (No. 252102231007), and the 111 project (No. D18023).

Declaration of competing interest

All the contributing authors report no conflict of interests in this work.

Author contribution statement

P. Y. K.: Writing – original draft. Y. K. Z.: Data curation, formal analysis. Q. X. S.: Validation. Z. Y. L.: Software, validation. Y. L. W.: Writing – review & editing, funding acquisition. H. L.: Resources, funding acquisition. C. T. L.: Project administration, funding acquisition. C. Y. S.: Conceptualization. All the authors have approved the final manuscript.

Use of AI statement

None.

References

[1] Meng, K.; Zhang, J. J.; Zhu, B. C.; Jiang, C. J.; García, H.; Yu, J. G. Interfacial charge transfer in ZnO/COF S-scheme photocatalyst via Zn–N bond. *Adv. Mater.* **2025**, *37*, 2505088.

[2] Li, D.; Cui, T. R.; Liu, J. H.; Shao, W. C.; Liu, X.; Chen, Z. K.; Xu, Z. G.; Li, X.; Xu, S. Y.; Xie, Z. Y. et al. Motion-unrestricted dynamic electrocardiogram system utilizing imperceptible electronics. *Nat. Commun.* **2025**, *16*, 3259.

[3] Wang, Q.; Guan, H.; Wang, C.; Lei, P. M.; Sheng, H. W.; Bi, H. S.; Hu, J. K.; Guo, C. H.; Mao, Y. C.; Yuan, J. et al. A wireless, self-powered smart insole for gait monitoring and recognition via nonlinear synergistic pressure sensing. *Sci. Adv.* **2025**, *11*, eadu1598.

[4] Yin, J.; Hinchet, R.; Shea, H.; Majidi, C. Wearable soft technologies for haptic sensing and feedback. *Adv. Funct. Mater.* **2021**, *31*, 2007428.

[5] Zhang, T. R.; Yu, J. T.; Guo, H. Y.; Qi, J. N.; Che, M. H.; Hou, M. C.; Jiao, P. X.; Zhang, Z. H.; Yan, Z. H.; Zhou, L. M. et al. Sapiential battery systems: Beyond traditional electrochemical energy. *Chem. Soc. Rev.* **2024**, *53*, 12043–12097.

[6] Jabri, M.; Masoumi, S.; Kandukuri, T. R.; Occhipinti, L. G. Flexible thin-film thermoelectric generators for human skin-heat harvesting: A numerical study. *Nano Energy* **2024**, *129*, 110001.

[7] Jia, Y. H.; Jiang, Q. L.; Sun, H. D.; Liu, P. P.; Hu, D. H.; Pei, Y. Z.; Liu, W. S.; Crispin, X.; Fabiano, S.; Ma, Y. G. et al. Wearable thermoelectric materials and devices for self-powered electronic systems. *Adv. Mater.* **2021**, *33*, 2102990.

[8] He, Y. Q.; Lin, X. Y.; Feng, Y.; Luo, B. H.; Liu, M. X. Carbon nanotube ink dispersed by chitin nanocrystals for thermoelectric converter for self-powering multifunctional wearable electronics. *Adv. Sci.* **2022**, *9*, 2204675.

[9] Chen, Z. Y.; Liu, S.; Kang, P. Y.; Wang, Y. L.; Liu, H.; Liu, C. T.; Shen, C. Y. Decoupled temperature–pressure sensing system for deep learning assisted human-machine interaction. *Adv. Funct. Mater.* **2024**, *34*, 2411688.

[10] Li, J. J.; He, X. Y.; Wang, J. H.; Zhu, S. Y.; Zhang, M. C.; Wu, C. X.; Dong, G. Y.; Liu, R. H.; Wang, L. M.; Chen, L. D. et al. Nanoarchitectonics of high-performance and flexible n-type organic-inorganic composite thermoelectric fibers for wearable electronics. *ACS Nano* **2025**, *19*, 11440–11449.

[11] Zhao, W.; Zheng, Y. W.; Huang, A. B.; Jiang, M.; Wang, L. J.; Zhang, Q. H.; Jiang, W. Metal-halogen interactions inducing phase separation for self-healing and tough ionogels with tunable thermoelectric performance. *Adv. Mater.* **2024**, *36*, 2402386.

[12] Yang, M. C.; Hu, Y.; Wang, X. L.; Chen, H.; Yu, J. T.; Li, W. Z.; Li, R. Y.; Yan, F. Chaotropic effect-boosted thermogalvanic ionogel thermocells for all-weather power generation. *Adv. Mater.* **2024**, *36*, 2312249.

[13] Liu, W.; Fang, Y.; Lyu, X. L.; Peng, X. F.; Luo, Z. Z.; Zou, Z. G. Construction and application of thermogalvanic hydrogels. *Soft Sci.* **2024**, *4*, 44.

[14] Lu, X.; Mo, Z. W.; Liu, Z. P.; Hu, Y. F.; Du, C. Y.; Liang, L. R.; Liu, Z. X.; Chen, G. M. Robust, efficient, and recoverable thermocells with zwitterion-boosted hydrogel electrolytes for energy-autonomous and wearable sensing. *Angew. Chem., Int. Ed.* **2024**, *63*, e202405357.

[15] Kim, S.; Kwon, J. H.; Bae, Y.; Kim, J.; Park, T.; Moon, H. C. Realizing a high-performance n-type thermogalvanic cell by tailoring the thermodynamic equilibrium. *Energy Environ. Sci.* **2024**, *17*, 8102–8110.

[16] Du, Z. J.; Li, L.; Shen, G. Z. An ultra-thin wearable thermoelectric paster based on structured organic ion gel electrolyte. *Nano-Micro Lett.* **2025**, *17*, 204.

[17] Dai, Y. L.; Wang, H. B.; Qi, K.; Ma, X.; Wang, M. T.; Ma, Z. Y.; Wang, Z. R.; Yang, Y. L.; Ramakrishna, S.; Ou, K. K. Electrode-dependent thermoelectric effect in ionic hydrogel fiber for self-powered sensing and low-grade heat harvesting. *Chem. Eng. J.* **2024**, *497*, 154970.

[18] Xu, Z. Y.; Lin, S. C.; Yin, Y. S.; Gu, X. K. Synergy between gelatin hydrogels and electrodes for adjustable and thermally stable ionic thermoelectric supercapacitors. *Chem. Eng. J.* **2024**, *493*, 152734.

[19] Li, X. Y.; Jia, J. C.; Dai, Y. Q.; Zhang, X. S.; Guan, L. F.; Zhang, D. H.; Wang, F.; Wang, Q. M.; Zeng, W. Advanced N-type ionic thermoelectric cells featuring bidirectional cationic anchoring strategy and REDOX electrode. *Adv. Energy Mater.* **2025**, *15*, 2500584.

[20] Yu, J.; Luo, M. Y.; Zhu, X. F.; Qing, X.; Wang, W.; Zhong, W. B.; Liu, Q. Z.; Wang, Y. D.; Lu, Y.; Li, M. F. et al. Bacterial Cellulose-based ionogels with synergistically enhanced mechanical and thermoelectric performances for low-grade heat harvesting. *Chem. Eng. J.* **2024**, *488*, 150638.

[21] Chen, Q. L.; Chen, B.; Xiao, S. H.; Feng, J. S.; Yang, J.; Yue, Q.; Zhang, X.; Wang, T. H. Giant thermopower of hydrogen ion enhanced by a strong hydrogen bond system. *ACS Appl. Mater. Interfaces* **2022**, *14*, 19304–19314.

[22] Fu, M.; Sun, Z. X.; Liu, X. B.; Huang, Z. K.; Luan, G. F.; Chen, Y. T.; Peng, J. P.; Yue, K. Highly stretchable, resilient, adhesive, and self-healing ionic hydrogels for thermoelectric application. *Adv. Funct. Mater.* **2023**, *33*, 2306086.

[23] Cheng, C.; Wang, S. J.; Tan, P.; Dai, Y. W.; Yu, J.; Cheng, R.; Feng, S. P.; Ni, M. Insights into the thermopower of thermally regenerative electrochemical cycle for low grade heat harvesting. *ACS Energy Lett.* **2021**, *6*, 329–336.

[24] Gao, C. T.; Lee, S. W.; Yang, Y. Thermally regenerative electrochemical cycle for low-grade heat harvesting. *ACS Energy Lett.* **2017**, *2*, 2326–2334.

[25] Han, C. G.; Qian, X.; Li, Q. K.; Deng, B.; Zhu, Y. B.; Han, Z. J.; Zhang, W. Q.; Wang, W. C.; Feng, S. P.; Chen, G. et al. Giant thermopower of ionic gelatin near room temperature. *Science* **2020**, *368*, 1091–1098.

[26] Li, N.; Wang, Z. S.; Yang, X. R.; Zhang, Z. Y.; Zhang, W. D.; Sang, S. B.; Zhang, H. L. Deep-learning-assisted thermogalvanic hydrogel E-skin for self-powered signature recognition and biometric authentication. *Adv. Funct. Mater.* **2024**, *34*, 2314419.

[27] Gui, J. X.; Cheng, Y.; Ren, K.; Liu, Z. P.; Zhu, Z. B.; Xue, Z. Y.; Zhu, Y. B.; Wang, R. H.; Pei, G.; Sui, J. et al. Development of ternary hydrogel electrolytes for superior gel thermocells: Exceptional anti-drying, anti-freezing, and mechanical robustness. *Adv. Mater.* **2025**, *37*, 2420214.

[28] Hu, J. D.; Wei, J. Y.; Li, J. M.; Bai, L.; Liu, Y.; Li, Z. G. Double selective ionic gel with excellent thermopower and ultra-high energy density for low-quality thermal energy harvesting. *Energy Environ. Sci.* **2024**, *17*, 1664–1676.

[29] Wang, Z. S.; Li, N.; Yang, X. R.; Zhang, Z. Y.; Zhang, H. L.; Cui, X. J. Thermogalvanic hydrogel-based e-skin for self-powered on-body dual-modal temperature and strain sensing. *Microsyst. Nanoeng.* **2024**, *10*, 55.

[30] Yu, B. Y.; Xiao, H.; Zeng, Y. L.; Liu, S. Y.; Wu, D. R.; Liu, P.; Guo, J. H.; Xie, W. K.; Duan, J. J.; Zhou, J. Cost-effective n-type thermocells enabled by thermosensitive crystallizations and 3D multi-structured electrodes. *Nano Energy* **2022**, *93*, 106795.

[31] Han, Y.; Zhang, J.; Hu, R.; Xu, D. Y. High-thermopower polarized electrolytes enabled by methylcellulose for low-grade heat harvesting. *Sci. Adv.* **2022**, *8*, eabl5318.

[32] Chai, Y. P.; Li, H. B.; He, Y. L.; Tian, J. Y.; Gu, Z. J.; Chi, X. D. Unlocking enhanced thermogalvanic cell performance via molecular chaperone-assisted non-toxic redox couple for waste heat harvesting. *Chem. Eng. J.* **2025**, *516*, 164170.

[33] Buckingham, M. A.; Zhang, S.; Liu, Y. Q.; Chen, J.; Marken, F.; Aldous, L. Thermogalvanic and thermocapacitive behavior of superabsorbent hydrogels for combined low-temperature thermal energy conversion and harvesting. *ACS Appl. Energy Mater.* **2021**, *4*, 11204–11214.

[34] Zhang, D.; Mao, Y.; Ye, F.; Li, Q.; Bai, P. J.; He, W.; Ma, R. J. Stretchable thermogalvanic hydrogel thermocell with record-high specific output power density enabled by ion-induced crystallization. *Energy Environ. Sci.* **2022**, *15*, 2974–2982.

[35] Zhou, Y. T.; Zhang, S.; Buckingham, M. A.; Aldous, L.; Beirne, S.; Wu, C.; Liu, Y. Q.; Wallace, G.; Chen, J. Novel porous thermosensitive gel electrolytes for wearable thermo-electrochemical cells. *Chem. Eng. J.* **2022**, *449*, 137775.

[36] Hong, S. H.; Hsu, C. C.; Liu, T. H.; Lee, T. C.; Tung, S. H.; Chen, H. L.; Yu, J.; Liu, C. L. Extremely large Seebeck coefficient of gelatin methacryloyl (GelMA)-based thermogalvanic cells by the dual effect of ion-induced crystallization and nanochannel control. *Mater. Today Energy* **2024**, *42*, 101546.

[37] Li, Y. S.; Wang, W. X.; Cui, X. J.; Li, N.; Ma, X. L.; Wang, Z. S.; Nie, Y. Y.; Huang, Z. Q.; Zhang, H. L. Self-powered machine-learning-assisted material identification enabled by a thermogalvanic dual-network hydrogel with a high thermopower. *Small* **2025**, *21*, 2405911.

[38] Yang, X. Y.; Wang, P.; Tang, X. Z.; Wang, Z. N.; Ye, J. H.; Duan, W.; Yue, Y.; Ci, T.; Liu, Y. P.; Ju, Y. Dual-modal hydrogels with synergistically enhanced mechanical-thermoelectric performance for intelligent wearable sensing and automotive temperature feedback systems. *Nano Energy* **2025**, *140*, 111057.

[39] Liu, Y.; Zhang, Q.; Odunmbaku, G. O.; He, Y. J.; Zheng, Y. J.; Chen, S. S.; Zhou, Y. L.; Li, J.; Li, M.; Sun, K. Solvent effect on the Seebeck coefficient of Fe^{2+}/Fe^{3+} hydrogel thermogalvanic cells. *J. Mater. Chem. A* **2022**, *10*, 19690–19698.

[40] Peng, P.; Li, Z.; Xie, D. B.; Zhu, K. H.; Du, C. Y.; Liang, L. R.; Liu, Z. X.; Chen, G. M. Aqueous eutectic hydrogel electrolytes enable flexible thermocells with a wide operating temperature range. *J. Mater. Chem. A* **2023**, *11*, 6986–6996.

[41] Luo, P.; Dong, S. Y.; Liang, L. R.; Kuang, F. X.; Du, C. Y.; Ye, Z. Q.; Chen, G. M. Highly sensitive thermoelectric fabric of PEDOT:PSS/SWCNT@PU composite fibers for body-temperature monitoring and fever alarming. *Adv. Mater.* **2026**, *38*, e18506.

[42] Fu, M.; Wu, Z. Z.; Liu, X. B.; Yuan, Y. W.; Lai, X. J.; Yue, K. Highly stretchable ionic hydrogels with enhanced thermoelectric performance and flame retardancy for intelligent fire protection. *J. Mater. Chem. A* **2024**, *12*, 27588–27597.

[43] Li, H. X.; Ding, Z. F.; Zhou, Q.; Chen, J.; Liu, Z. X.; Du, C. Y.; Liang, L. R.; Chen, G. M. Harness high-temperature thermal energy via elastic thermoelectric aerogels. *Nano-Micro Lett.* **2024**, *16*, 151.

[44] Li, G.; Hu, Y.; Chen, J. H.; Liang, L. R.; Liu, Z. X.; Fu, J.; Du, C. Y.; Chen, G. M. Thermoelectric and photoelectric dual modulated sensors for human internet of things application in accurate fire recognition and warning. *Adv. Funct. Mater.* **2023**, *33*, 2303861.

[45] Zong, Y. D.; Li, H. B.; Li, X.; Lou, J.; Ding, Q. J.; Liu, Z. Q.; Jiang, Y. F.; Han, W. J. Bacterial cellulose-based hydrogel thermocells for low-grade heat harvesting. *Chem. Eng. J.* **2022**, *433*, 134550.

[46] Liu, L. L.; Zhang, D.; Bai, P. J.; Mao, Y.; Li, Q.; Guo, J. Q.; Fang, Y. J.; Ma, R. J. Strong tough thermogalvanic hydrogel thermocell with extraordinarily high thermoelectric performance. *Adv. Mater.* **2023**, *35*, 2300696.

[47] Duan, J. J.; Feng, G.; Yu, B. Y.; Li, J.; Chen, M.; Yang, P. H.; Feng, J. M.; Liu, K.; Zhou, J. Aqueous thermogalvanic cells with a high Seebeck coefficient for low-grade heat harvest. *Nat. Commun.* **2018**, *9*, 5146.

[48] Liu, L. L.; Zhang, D.; Bai, P. J.; Fang, Y. J.; Guo, J. Q.; Li, Q.; Ma, R. J. Fatigue-resistant and super-tough thermocells. *Nat. Commun.* **2025**, *16*, 1963.